Science Advances

AAAS

advances.sciencemag.org/cgi/content/full/3/10/e1701247/DC1

Supplementary Materials for

Biosensing near the neutrality point of graphene

Wangyang Fu, Lingyan Feng, Gregory Panaitov, Dmitry Kireev, Dirk Mayer, Andreas Offenhäusser, Hans-Joachim Krause

Published 25 October 2017, *Sci. Adv.* **3**, e1701247 (2017)
DOI: 10.1126/sciadv.1701247

This PDF file includes:

section S1. Single-crystal monolayer CVD graphene

Figure S1A gives an optical image of the single crystal CVD graphene grown on copper foils. Figure S1 (B and C) show the corresponding Raman spectra before and after transfer onto a SiO_2/Si substrate, respectively. The intensity ratio $I_{2D}/I_G>2$ confirms the single layer nature of the as-grown and as-transferred graphene. The absence of the disorder D peak (at around 1350 cm^{-1}) in the Raman spectra suggests a high quality of our samples.

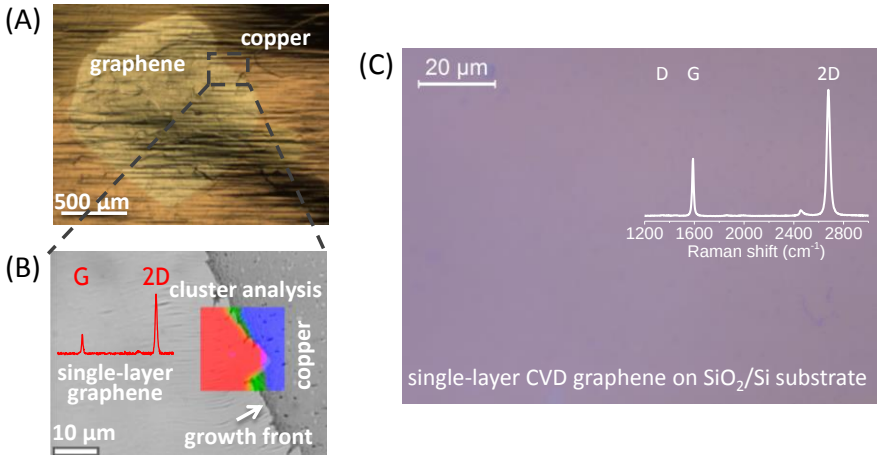

fig. S1. High-quality single-crystal CVD graphene. (**A**) CVD growth of millimeter-sized hexagon-shaped graphene single crystals on copper foils: 4 h (size: ~1.2 mm). The contrast in the optical images comes from the oxidation of uncovered copper (reddish, CuO_X). (**B**) Raman cluster analysis: red area represents high-quality single-layer graphene (with typical G and 2D band but without D band, see the Raman spectra in red line); green area represents graphene edges (growth front) contain D band in the spectra (not show); blue area is the copper substrate. (**C**) An optical image of as-transferred graphene on SiO_2/Si substrate. Inset: The typical Raman spectra confirms the quality of the transferred single-layer graphene with negligible D band.

section S2. Electrochemical cleaning of graphene: Basic principle

Potential surface contaminations of graphene include metal or metal oxide leftovers, polymer residues, and hydrocarbon adsorptions introduced during device processing and storage (fig. S2) (*34-36*). These contaminants not only degrade the electrical performance of GFETs, but also block graphene surface for further functionalization, and thus seriously jeopardizing the potential of graphene devices as potent biochemical sensors.

In this study we adopted a mild cyclic liquid gate voltage that when applied to a GFET very rapidly removes its surface contaminants: i) metal or metal oxide leftovers can be effectively oxidized and dissolved into solution during repeating electrochemical processes using the graphene surface as anode (*22*); ii) particularly, previous literature provided the thermodynamic and electrochemical basis to electrochemically remove or decompose carbonaceous impurities, amorphous carbon, and hydrocarbon-like acetylene black in salt solutions (otherwise non-spontaneous chemical reaction) (*23*, *24*). These highly disordered carbons are more readily oxidized electrochemically than carbon nanotubes or graphene.

As schemed in fig. S2, in order to further accelerate the electrochemical processes, a sine wave V_{ac} with amplitude A_{ac}=70.7 mV at frequency f=77.77 Hz was superimposed on the liquid gate as we sweep the DC gate voltage V_{GS} from negative to positive (and reversely). This electrostatic-assisted electrochemical cleaning technique yields consecutively recovered transfer curves of the GFET-I as shown in Fig. 1D (in the main text), suggesting a surface refreshment of graphene.

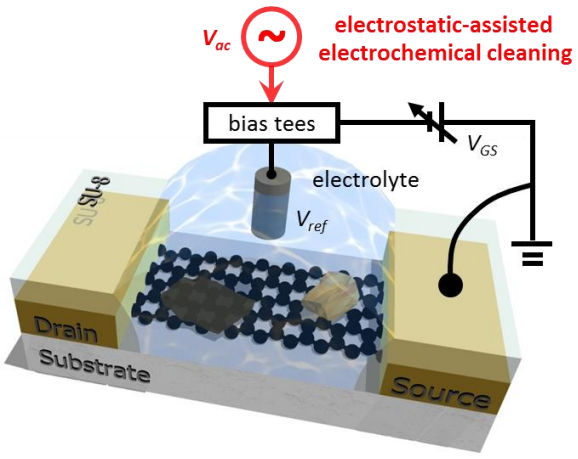

fig. S2. Schematic presentation of in situ electrochemical cleaning of an electrolyte-gated GFET device. Inset, possible contaminants on graphene surface, including Cu residues and amorphous carbon (α-C:H). These contaminants can be rapidly removed by using electrostatic-assisted electrochemical cleaning technology introduced in this study.

section S3. Noise characterizations

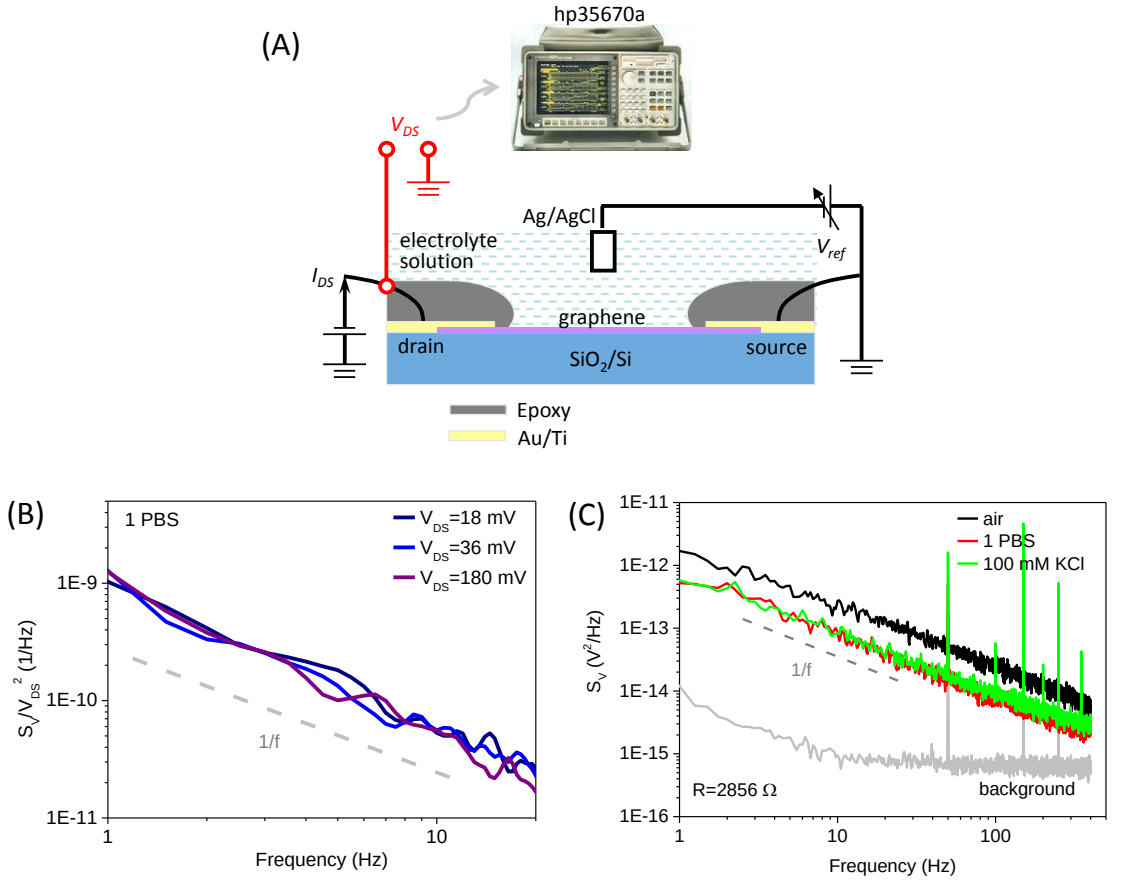

fig. S3. Electronic noise characterization for graphene on SiO_2/Si substrate. (**A**) A schematics for electronic noise characterization in graphene. (**B**) The normalized power spectral density (PSD) $S_V(f)/V_{DS}^2$ of an electrolyte-gated GFET at different V_{DS}. All the curves exhibit a clear $1/f$ dependence, as indicated by the dashed gray line. The normalized PSD $S_V(f)/V_{DS}^2$ satisfactorily overlaps according to Hooge's empirical law. (**C**) The PSD $S_V(f)$ of another GFET device tested in different environments with resistance R=2856 Ω. The corresponding thermal (and amplifier) background noise recorded at zero bias (gray line), has been subtracted from all the data.

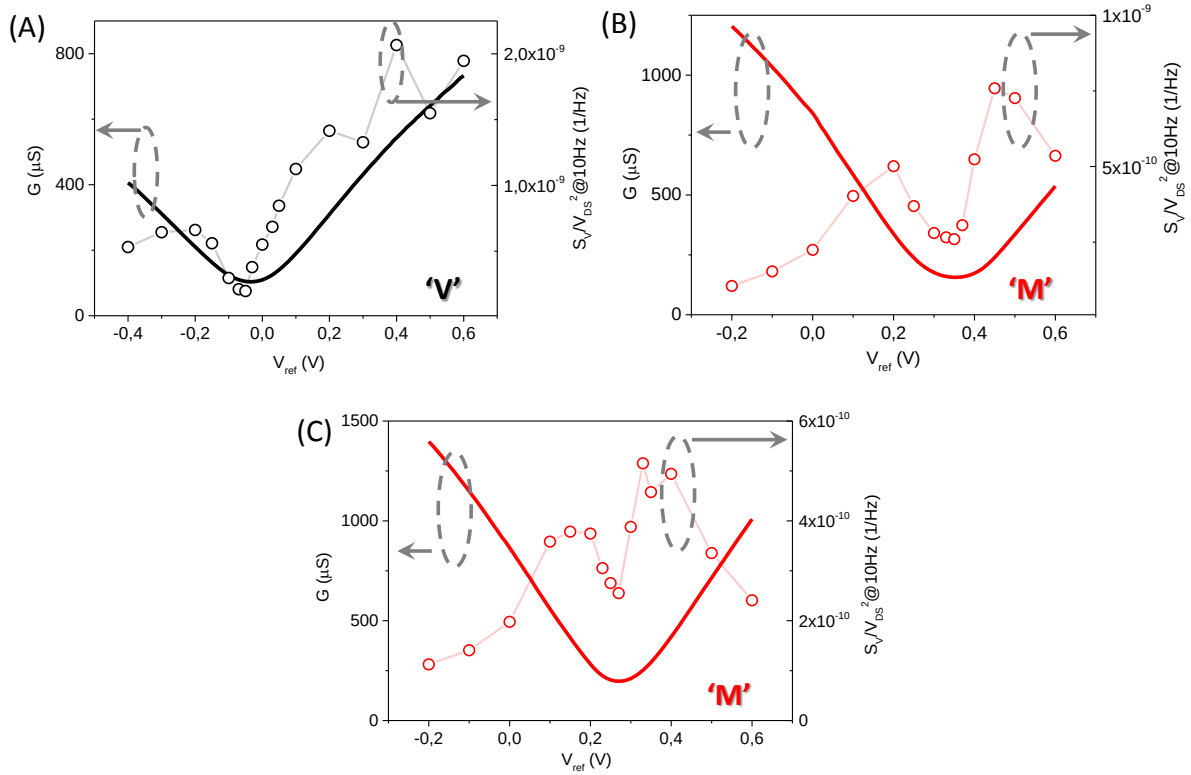

fig. S4. Electronic noise characterization for graphene on Si_3N_4/Si and sapphire substrates. (**A**) The $G(V_{ref})$ curves (to the left axis) and the corresponding "V"-shaped normalized PSD S_V/V_{DS}^2 (at f=10 Hz with a bandwidth of 1Hz, to the right axis) for a typical GFET device fabricated on Si_3N_4/SiO_2/Si substrate after electrostatic-enforced electrochemical cleaning. The field-effect mobility of this device was estimated to be ~550 cm^2/Vs for both hole and electron carriers. (**B**) and (**C**) depict the $G(V_{ref})$ curves (to the left axis) and the corresponding "M"-shaped normalized PSD S_V/V_{DS}^2 (at f=10 Hz with a bandwidth of 1 Hz, to the right axis) for two typical GFET devices fabricated on sapphire substrate after electrostatic-assisted electrochemical cleaning. The field-effect mobilities of the device shown in (**B**) and (**C**) were estimated to be ~1000 cm^2/Vs and ~1500 cm^2/Vs for both hole and electron carriers, respectively. The device fabricated on sapphire substrate had experienced two neuronal cultures and one HL-1 cell culture (with altogether up to 14 days). Prior to the electrochemical cleaning, these GFET devices were treated in Terg-a-zyme enzyme detergent for 1 hour to remove the cells followed by a thorough rinse in DI water.

section S4. SNR in conventional operated GFETs

In fig. S5, we find that in a conventional GFET optimal SNRs can be achieved close to the point of (~80-90 %) the maximum transconductance, normally at the outmost points of the neutrality region.

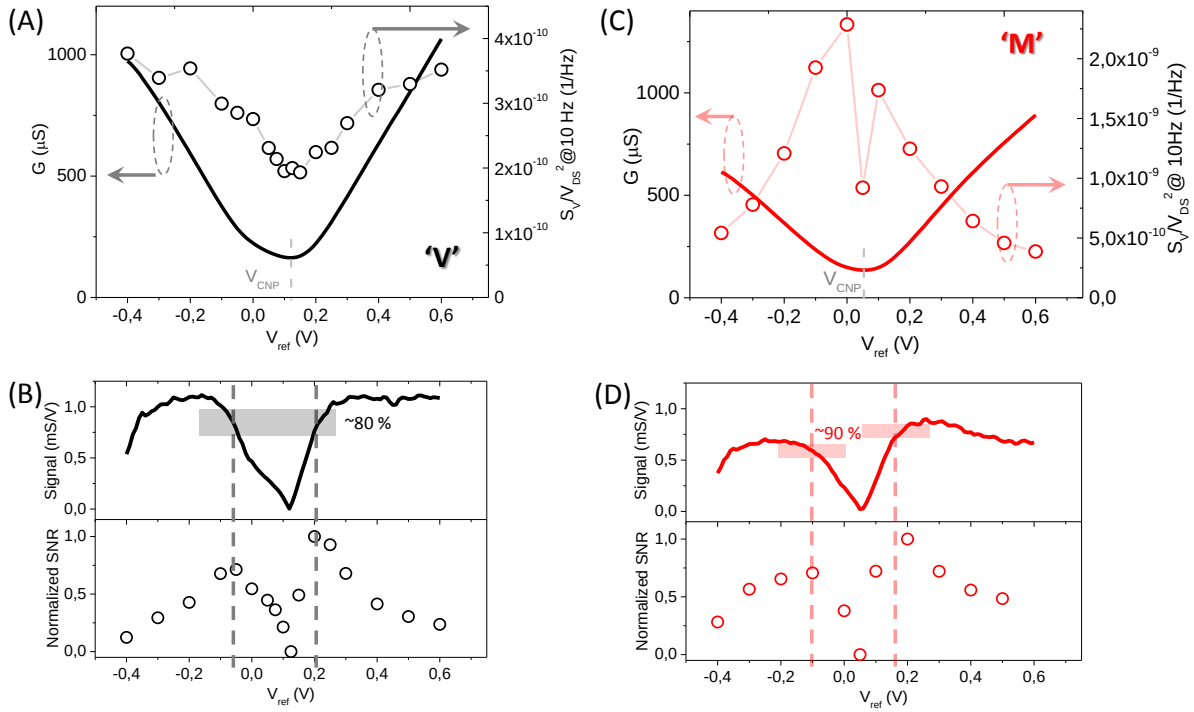

fig. S5. SNR in conventional operated GFET devices. (**A**) The $G(V_{ref})$ curves (to the left axis) and the corresponding "V"-shaped normalized PSD S_V/V_{DS}^2 (at f=10 Hz with a bandwidth of 1 Hz, to the right axis) for GFET-I after preliminary electrostatic-enforced electrochemical cleaning. (**B**) The derived transconductance of GFET-I (upper panel) and the calculated SNR at different V_{ref}. An optimal SNR is achieved before the transconductance reaches its maximum (at ~80 %). (**C**) The $G(V_{ref})$ curves (to the left axis) and the corresponding "M"-shaped normalized PSD S_V/V_{SD}^2 (at f=10 Hz with a bandwidth of 1 Hz, to the right axis) for another GFET-III (also fabricated on a SiO_2/Si substrate) after preliminary electrostatically-enforced electrochemical cleaning. (**D**) The derived transconductance of GFET-III (upper panel) and the calculated SNR at different V_{ref}. An optimal SNR is achieved before the transconductance reaches its maximum (at ~90 %).

section S5. pPNA-DNA hybridization: 1-base mismatched

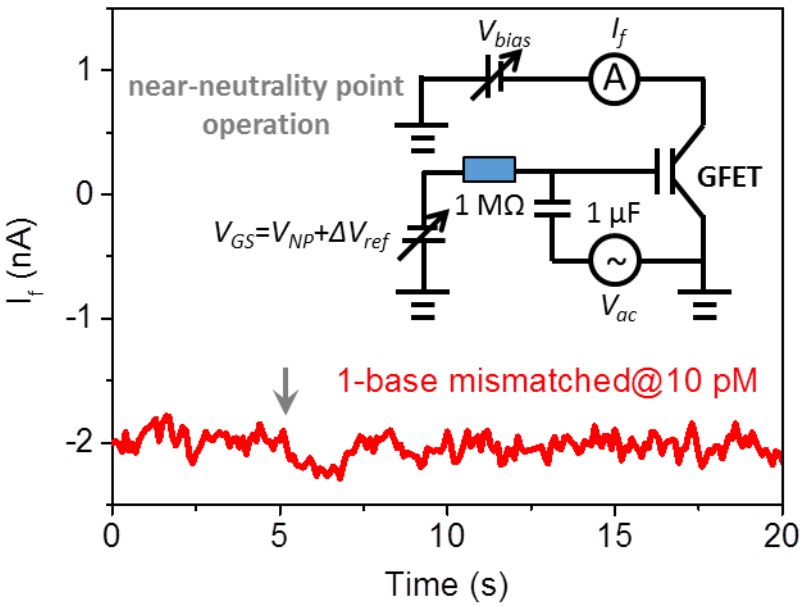

fig. S6. No obvious changes in I_f of the graphene biosensor versus time upon the introduction of 10 pM 1-base–mismatched ssDNA in 1 mM PBS solution. Inset: the circuit diagram of the ambipolar GFET operated near its neutrality point.